



Sonochemical synthesis of NiCo₂O₄/NRGO nanocomposite as a cathodic material for the electrochemical capacitor application

Shahed Hassanpoor¹ · Farzaneh Aghely¹

Received: 25 June 2020 / Accepted: 3 October 2020 / Published online: 19 October 2020
© Iranian Chemical Society 2020

Abstract

In this work, a novel nanocomposite consisting of NiCo₂O₄/N-doped reduced graphene oxide was prepared. In the first step, ultrafine NiCo₂O₄ nanoparticles (4.4 nm) were synthesized by the sonochemical method. In the second step, graphene oxide was synthesized by modified Hummer methods and then reduced and N-doped (NRGO) by a chemical method using a mixture of hydrazine and ammonia solution. NiCo₂O₄/NRGO nanocomposite was produced using the dispersion of NRGO nanosheets and NiCo₂O₄ nanoparticles under ultrasonic radiation for 30 min. The structure, morphology, and composition of various samples were investigated using an adequate analytical characterization method. Electrochemical tests such as cyclic voltammetry and galvanostatic charge–discharge studies were done in a three-electrode system with 1.0 M Na₂SO₄ solution as the electrolyte for supercapacitive study of the samples. The results confirmed the excellent supercapacitive behavior of the nanocomposite and good stability during the charge–discharge cycle. The specific capacitance for the nanocomposite was calculated using a galvanostatic charge–discharge experiment which 618 F.g⁻¹ in current density of 4.0 A.g⁻¹.

Keywords Sonochemical · NiCo₂O₄ · Nanocomposite · Supercapacitor

Introduction

Increasing demand for high-efficiency, renewable energy sources has led to many studies of modern electrode materials for energy storage in devices such as batteries and supercapacitors (SCs) [1]. The modification of the electrodes with nanomaterials in supercapacitors has resulted in much higher surface areas, much thinner dielectrics that decrease the distance between the electrodes, and easy mass transport of electrolyte ions in the electrochemical process [2]. The major advantage of supercapacitors is their higher power densities than batteries and conventional dielectric capacitors. The efficiency of supercapacitors is strongly dependent on the materials used in the preparation of the electrodes. So a lot of research has been done in this area, and it is still going on. Some of the metal oxide electrode materials used in supercapacitors are RuO₂, MnO₂, NiO, Ni(OH)₂, Fe₃O₄, Co(OH)₂, Co₃O₄ [3]. Among these, metal

oxides appear to be attractive in terms of its high theoretical capacity, low toxicity, natural abundance, and environment friendliness [4]. The three main categories of supercapacitors are electrochemical double-layer capacitor (EDLC), pseudocapacitor, and hybrid type. The mechanism of EDLCs is the separation of the electrostatic charge from the electrolyte on the electrode surface. In contrast, the mechanism in pseudocapacitors is due to faradaic redox reaction in the internal structure and surface of the electrode material [5]. The NiCo₂O₄ has shown better electrical and mechanical properties than the single-component metal oxides Co₃O₄ and NiO [6]. The porous structure of NiCo₂O₄ is also one more appealing approach to overcome the volume changes and enhance capacity retention because of more electroactive sites for redox reactions [7]. There are many methods for the synthesis of NiCo₂O₄ such as sol–gel [8, 9], hydrothermal [10, 11], electrodeposition [12], and microwave-assisted synthesis [13].

Nowadays, nanomaterials have received much attention due to their amazing properties such as high surface area and convenience of surface modification [14, 15]. Nowadays, two-dimensional (2D) nanomaterials such as graphene with sp² hybridized carbon atoms have been of interest because

✉ Shahed Hassanpoor
Shahed_Hassanpoor110@yahoo.com;
S_Hassanpoor@guilan.ac.ir

¹ Department of Nanotechnology, Faculty of Engineering,
University of Guilan, Rasht, Iran

of its excellent mechanical, electrical, and thermal properties and large lateral lengths [16, 17].

In the present work, fine NiCo_2O_4 nanoparticles were synthesized with a novel straightforward, novel, and fast sonochemical synthesis. Graphite oxide was synthesized by the modified Hummers method. The graphite oxide then reduced and N-doped graphene by a chemical method using hydrazine and NH_3 solution. The $\text{NiCo}_2\text{O}_4/\text{NRGO}$

nanocomposite was successfully synthesized with ultrasound radiation and used for supercapacitor application on the carbon past substrate for the first time. The samples were characterized using Fourier-transform infrared (FT-IR), X-ray diffraction (XRD), scanning electron microscopy (SEM), and energy-dispersive X-ray spectroscopy (EDX) mapping methods. The cyclic voltammetry (CV), galvanostatic charge–discharge (GCD), and electrochemical impedance

Fig. 1 The FT-IR spectrum of GO **a**, NRGO **b**, NiCo_2O_4 **c**, and the nanocomposites **d**

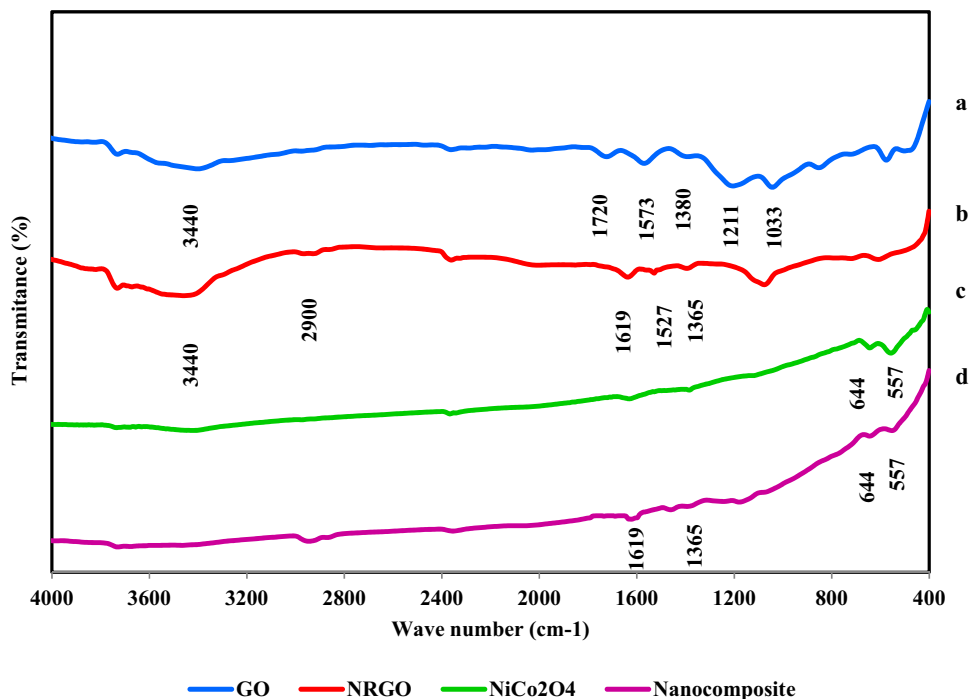
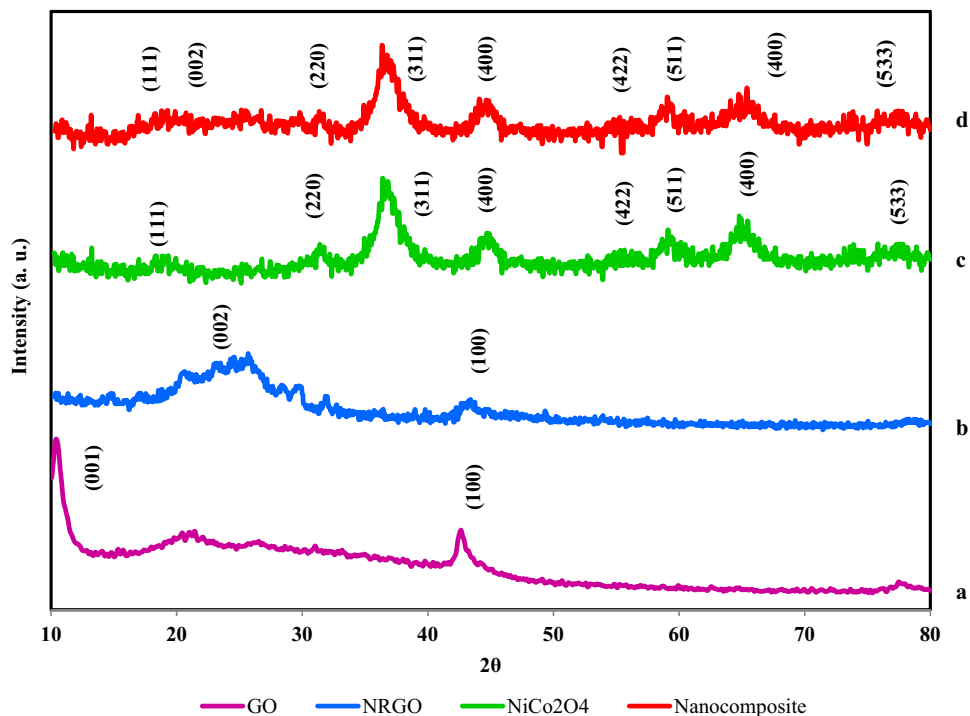


Fig. 2 The XRD patterns of GO **a**, NRGO **b**, NiCo_2O_4 **c**, and the nanocomposite **d**



spectroscopy (EIS) tests were used for capacitance study of the materials. Preparation of very fine particles using a combination of sonochemical and surfactant-assisted synthesis method at a much lower temperature and time than the reported methods and gained acceptable capacity are important points of the present study.

Materials and methods

Instrumentation

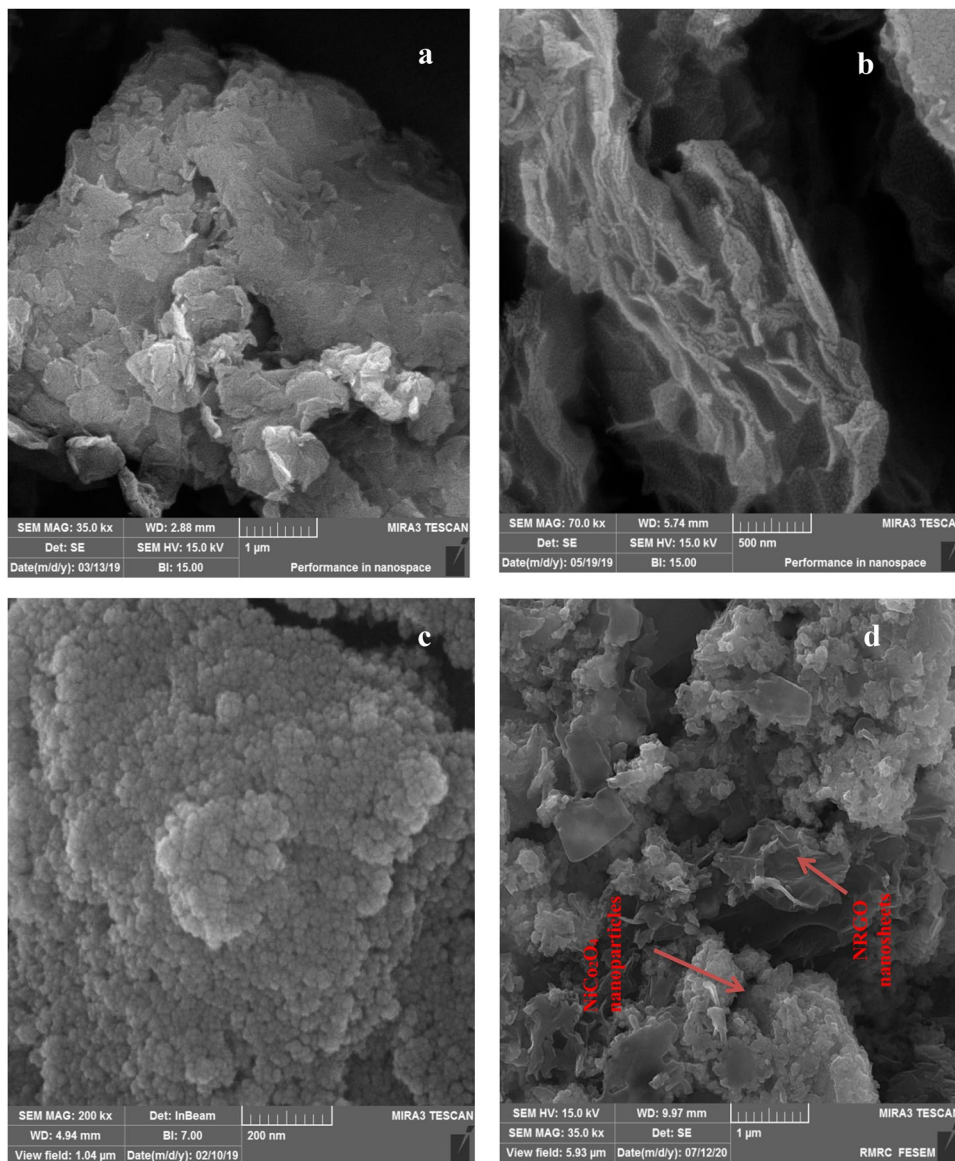
Electrochemical experiments were done in a cell of three electrodes with an Ag/AgCl (in saturated KCl) as a reference electrode, and a Pt wire was used as an auxiliary electrode with a PGSTAT 302 N instrument (Autolab, NOVA software equipped, the Netherlands). Crystallographic

characterization of the material was done by XRD measurements with an STOE-STADI diffractometer (Germany, $\lambda_{Cu} = 1.54 \text{ \AA}$). Morphological analysis was done with a field emission scanning electron microscopy (TESCAN, VEGA3, Czech Republic). An ultrasonic bath (SIGMA SONIC, 4 L, 100 W, Iran) was applied to synthesize the dispersion process. Fourier-transform infrared spectra (FT-IR) were recorded with an infrared spectrometer (Bruker, Alpha, KBr disk, Germany). The hydrothermal synthesis was done with a 70 ml Teflon-lined autoclave.

Chemicals and reagents

Graphite powder, $\text{Ni}(\text{NO}_3)_2 \cdot 6\text{H}_2\text{O}$, $\text{Co}(\text{NO}_3)_2 \cdot 6\text{H}_2\text{O}$, HCl, H_2O_2 , H_2SO_4 , NH_3 , urea, CTAB, hydrazine monohydrate, Na_2SO_4 , dimethylformamide (DMF), and ethanol from Merck were used as received. Nafion (5 wt% in ethanol,

Fig. 3 The FE-SEM GO **a**, NRGO **b**, NiCo_2O_4 **c** and the nanocomposites **d**



Sigma-Aldrich) was used for electrode preparation. Other salts and solvents were of analytical grade and were purchased from Merck. Daily solutions were prepared with doubly distilled deionized water.

Synthesis of NiCo₂O₄ nanoparticles

The synthesis process of NiCo₂O₄ nanoparticles has been done by a new process with a combination of heating in a water bath in the presence of carbonate, urea, surfactant, and ultrasound radiation which has resulted in the production of very fine particles. For this reason, 0.145 g Ni(NO₃)₂·6H₂O, 0.291 g Co(NO₃)₂·6H₂O, 0.36 g urea, and 0.15 g CTAB were added to 50 ml doubly distilled deionized water in a 100 mL beaker. The beaker was then placed in the ultrasonic bath. After this, a 20 mL solution of 0.047 mol L⁻¹ Na₂CO₃ was added dropwise to the above mixture using a syringe in 10 min under ultrasonic radiation and kept it in this condition for 15 min more. The temperature of the ultrasonic bath was fixed at 65 ± 3 °C. The purple precipitate was filtered and washed with 5.0 mL distilled water and ethanol twice alternately after cooling down to room temperature. Then, the precipitate was dried at 80 °C for 3 h. It was then transferred to the furnace and stored at 300 °C for 3 h for final calcination and converted to black NiCo₂O₄ nanoparticles powder.

Synthesis of N-doping reduced graphene oxide nanosheets (NRGO)

Modified Hummers method was applied for the synthesis of graphene oxide (GO) from graphite powder based on previously published articles [18, 19]. The graphene oxide suspension (100 ml distilled water, 0.04 g GO) was generated using sonication for 30 min in a sealed 250-mL round-bottom flask. Then, 50 μL of 100% N₂H₄·H₂O and 1 ml of 25% NH₃ were added to the above suspension and kept it at 95 °C for 60 min in the absence of any stirring using a water bath. The mixture was cooling down to 60 °C and then transferred to the Petri dish. After drying at 50 °C for 24 h in an oven, the black powder of NRGO nanosheets was prepared [20, 21].

Preparation of NiCo₂O₄/NRGO nanocomposite

The NiCo₂O₄/NRGO nanocomposite was synthesized with a convenient sonication method by the dispersion of 0.0045 g NRGO and 0.0105 g NiCo₂O₄ in a mixture of H₂O/C₂H₅OH(4:36 mL) for 30 min in the ultrasonic bath. The solvent was dried at 50 °C for 6 h. The adsorption of

NiCo₂O₄ nanoparticles on the NRGO nanosheets is based on van der Waals interactions.

Electrochemical study

To make the carbon paste, 18 mg of the graphite powder with 45 μL of silicone oil was mixed and then heated on the hotplate with stirring by a spatula for 15 min at 60 °C. Then, the above past is filled in a homemade Teflon electrode cavity (3 mm) by a spatula. A copper wire rod is attached to the sample from the back and pressed down. The electrode is then polished with a piece of paper to shine. It is then stored in an oven for 12 h at 60 °C. The active material ink was prepared from 30 μL Nafion solution, 15 mg sample, and 3 mL ethanol. 3 × 5 μL of active material ink (equal to 72.2 μg of active material, loading mass, 1 mg cm⁻²) was used to modify a freshly polished electrode by casting method after sonication for 10 min. The electrode dryness was done at 40 °C for 30 min. The key

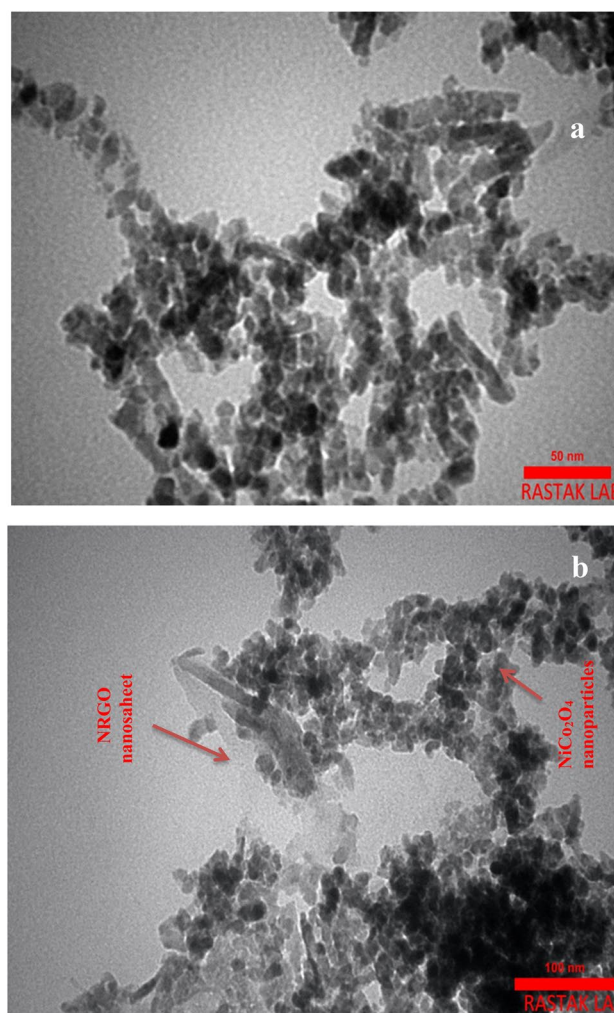


Fig. 4 The TEM image of the NiCo₂O₄ nanoparticles **a**, and the nanocomposites **b**

benefits of carbon paste electrodes include low cost, simple design, low background current, ability to introduce various modifiers during paste preparation, easy removal of electrode surface layer, low ohmic resistance, wide potential range [22]. CV and GCD experiments were done in 1 M Na₂SO₄ solution as the electrolyte. EIS and CV study in 10 mM K₄Fe(CN)₆ and 0.1 M KCl also was investigate for the samples. The GCD study was applied to determine the capacitance performance of active materials. The specific capacitance (SC) in F g⁻¹ dimensional was calculated from the following equation:

$$SC = \frac{I\Delta t}{m\Delta V}$$

where I, Δt, and ΔV are the discharge current (A), the discharge time (s), and the discharge potential range (V),

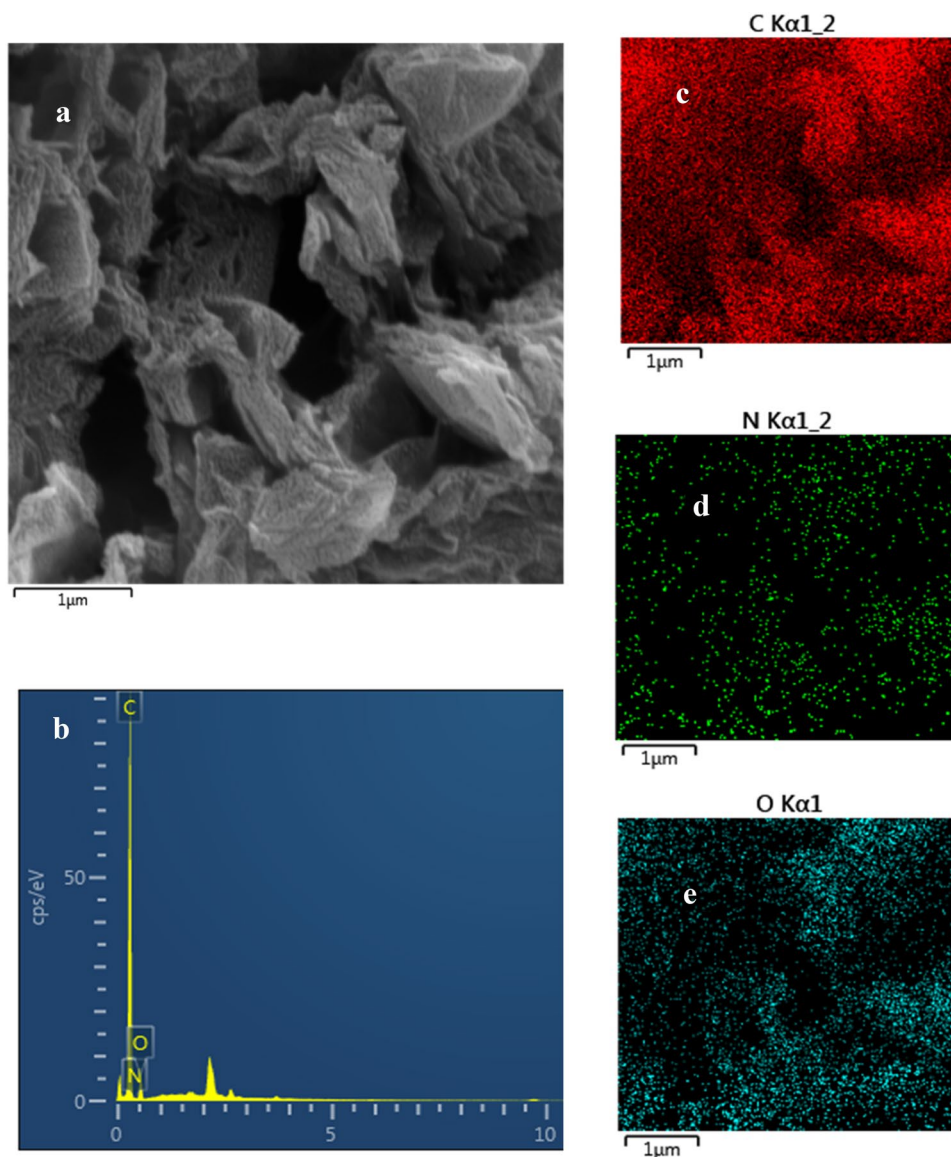
respectively, and the m (g) represents the mass of the active materials of the electrode [23].

Results and discussion

Material characterizations

Material characterization was done with FT-IR, XRD, FE-SEM, and EDX methods. FT-IR spectroscopy is a convenient and efficient analysis for the characterization of a functionalized nanoparticle and manufacturing bonds of nanoparticles. So, firstly the structure of GO, NRGO, NiCo₂O₄, and nanocomposite was characterized by FT-IR spectroscopy. In the GO FT-IR spectrum (Fig. 1a), different

Fig. 5 EDS spectrum of NRGO with its elemental distribution

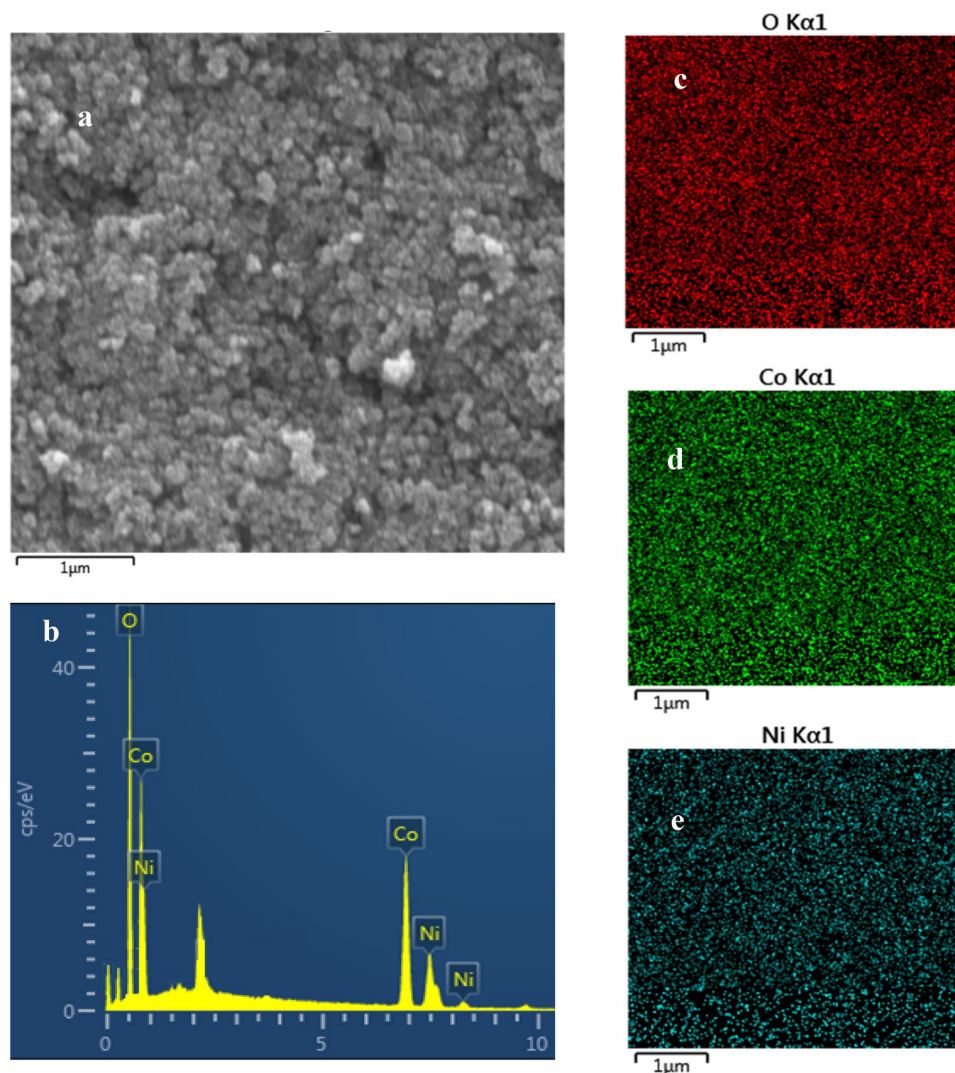


types of functional groups including oxygen are observed. In the region of $3000\text{--}3600\text{ cm}^{-1}$, broadband due to the O–H stretching vibration of hydroxyl groups was observed. The peak at 1720 cm^{-1} is due to C=O vibration. The peaks at 1380 cm^{-1} , 1211 cm^{-1} , and 1033 cm^{-1} are due to O–H deformation and C–OH stretching vibration and C–O stretching, respectively. The peak at 1573 cm^{-1} denotes the C=C band vibration of GO [19, 24]. The FT-IR spectrum of NRGO (Fig. 1b) was shown. The elimination of the C=O peak at 1720 cm^{-1} and intensity reduction of oxygen-containing peaks confirm successful synthesis of NRGO. The broad peak at 3440 cm^{-1} is related to the stretching of hydroxyl. The peaks at 2946 and 2885 cm^{-1} denote graphene sheet edges C–H bonds. The new weak peaks at 1527 and 1365 cm^{-1} are due to the C=N and C–N stretching vibration, confirming N-doping on the RGO nanosheets. The peak at 1619 cm^{-1} is due to C=C stretching vibration [20, 26]. Figure 1c shows the FT-IR of NiCo_2O_4 . The sharp bands at 557 and 644 cm^{-1} are due to Ni–O and Co–O vibration at

octahedral and tetrahedral sites, respectively [26, 26, 26]. Figure 1d shows the FT-IR spectrum of NiCo_2O_4 and NRGO nanocomposite. As can be seen, the peaks corresponding to both NiCo_2O_4 and NRGO were observed in the nanocomposite. These results confirmed the successful synthesis of the materials.

X-ray diffraction analysis (XRD) is the most effective method for the structure and size of a crystalline nanoparticle. The XRD patterns of GO, NRGO, NiCo_2O_4 , and nanocomposite are illustrated in Fig. 2. Figure 2a shows the XRD pattern of GO. The strong peak at $2\theta = 10.6^\circ$ attributes to the (001) plane reflection. Based on this peak, the spacing between the layers (0.85 nm) is much more than the natural graphite (0.34 nm), which confirms the successful entry of different forms of oxygen (hydroxyl, epoxy, and carbonyl) into the interlayer space of GO [26]. In the XRD pattern of NRGO (Fig. 2b), the peak at $2\theta = 10.6^\circ$ was eliminated, but a novel broad peak at around $2\theta = 24^\circ$ was observed due to (002) plane and approved GO nanosheets reduction. The

Fig. 6 EDS spectrum of NiCo_2O_4 with its elemental distribution



peak at $2\theta = 42.8^\circ$ is due to the (100) plane in the carbon hexagonal structure [26]. All the peaks in Fig. 2c correspond exactly to the spinel structure of NiCo_2O_4 . The X-ray diffraction characteristic peaks at $2\theta = 18.9, 31.2, 36.7, 44.6, 55.4, 59.1, 64.9,$ and 77° correspond to planes of spinel NiCo_2O_4 (JCPDS No. 20–0781) [26, 26]. No peak is observed at other angles, indicating the high purity of the synthesized material. The broad diffraction peaks reveal the small size of the products.

Estimated nanocrystallites size based on Scherrer's law from the (311) line also was done [26]:

$$d = 0.9\lambda / 0\beta_{1/2}\cos\theta$$

where λ is the wavelength of the X-ray source, $\beta_{1/2}$ is the half-height width of the diffraction peak (measured in radians), and θ is the diffraction angle. Based on this equation, the nanocrystallites size was 4.4 nm. The $\text{NiCo}_2\text{O}_4/\text{NRGO}$ nanocomposite XRD pattern is shown in Fig. 2d. As can be seen, all major peaks of the pure material are observed

precisely in the nanocomposite. The broad peak in the region $20\text{--}25^\circ$ can be attributed to NRGO nanosheets.

The morphological characterization of GO, NRGO, NiCo_2O_4 , and nanocomposites was done by FE-SEM (Fig. 3). Figure 3a, b exhibits the layered sheet nanostructure of GO and NRGO. The NiCo_2O_4 nanoparticles (Fig. 3c) have a very fine size (< 10 nm) with good monodispersity. This result has good agreement with XRD analysis for estimation of the size of nanoparticles. Figure 3d shows FE-SEM images of $\text{NiCo}_2\text{O}_4/\text{NRGO}$ nanocomposite. The contact between NRGO nanosheets and NiCo_2O_4 nanoparticles is seen, which is very necessary for the supercapacitor due to the conductivity enhancement. For a more detailed study of the surface morphology of NiCo_2O_4 nanoparticles and $\text{NiCo}_2\text{O}_4/\text{NRGO}$ nanocomposite sample, the TEM images were also investigated and the close contact between NRGO nanosheets and NiCo_2O_4 nanoparticles is approved (Fig. 4).

The chemical composition of the NRGO and NiCo_2O_4 nanostructures has been analyzed using EDS (Figs. 5, 6). Figure 5c, d, e represents the homogeneous distribution

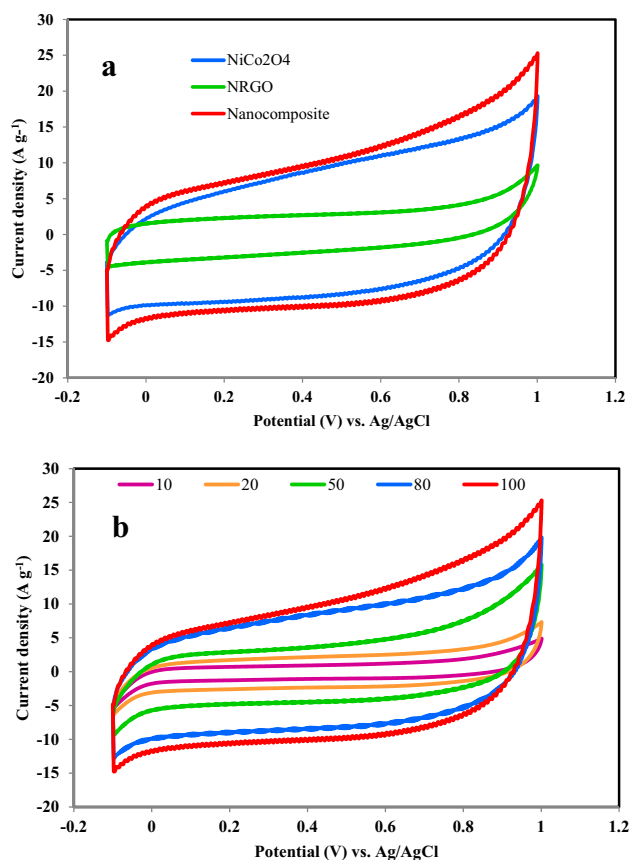


Fig. 7 The CV curves of NRGO, NiCo_2O_4 , and nanocomposite at 100 mV s^{-1} **a** and the CV curves of the $\text{NiCo}_2\text{O}_4/\text{NRGO}$ nanocomposite electrode at various scan rates ranged from 10 to 100 mV s^{-1} **b**

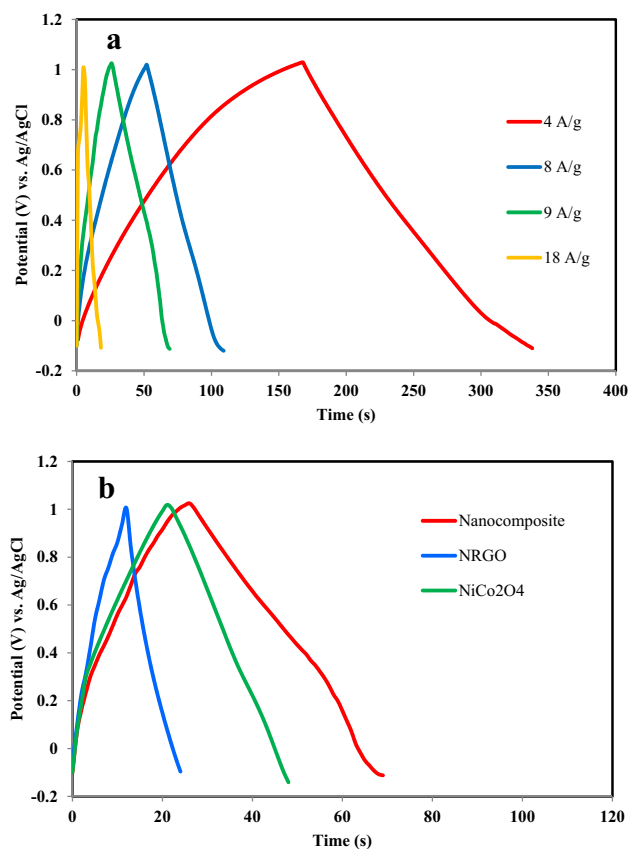


Fig. 8 The GCD curve of the nanocomposite with several current densities up to 9 A g^{-1} **a** and the GCD test of NRGO, NiCo_2O_4 , and the nanocomposite with an applied constant current density of 9 A g^{-1} to investigate **b**

of nitrogen (N), oxygen (O), and carbon (C) elemental mapping in NRGO systems. The nitrogen presence confirmed the successful synthesis of nitrogen-doped RGO. EDS analysis of NiCo_2O_4 along with its elemental mapping is shown in Fig. 6. The homogenous distribution of Ni, Co, and O elements has to be seen in the sample, and the Co has more strength signals than Ni. These results confirmed the successful synthesis of the samples.

Electrochemical capacity study

The electrochemical capacitive studies of the materials and fabricated working electrodes are carried out as mentioned in the general procedure. The CVs were recorded in the -0.1 to 1.0 V potential window at different scan rates in the 1 M Na_2SO_4 electrolyte. Figure 7a shows CV curves of NRGO, NiCo_2O_4 , and nanocomposite at 100 mV s^{-1} . The CV curve for the NRGO electrode is almost ideally rectangular illustrating the EDLC mechanism [26]. The CV of NiCo_2O_4 is relatively rectangular with slight redox peaks indicating the electrochemical reversible reaction and its supercapacitive property [26, 26]. The integrated area of the CV of NiCo_2O_4 ($17.35 \text{ A} \cdot \text{V} \cdot \text{g}^{-1}$) is significantly larger than NRGO ($5.42 \text{ A} \cdot \text{V} \cdot \text{g}^{-1}$) because of its faradic capacitance. The CV curve of the $\text{NiCo}_2\text{O}_4/\text{RGO}$ nanocomposite was exhibited as the largest area ($21.01 \text{ A} \cdot \text{V} \cdot \text{g}^{-1}$) compared to the pure materials indicating the good conductivity and capacitance for it. Figure 7b shows the CV curves of the $\text{NiCo}_2\text{O}_4/\text{NRGO}$ nanocomposite electrode from 10 to 100 mV s^{-1} of scan rates. The ideal and symmetrical rectangular shape is found throughout the potential window even at a low scanning rate, indicating its high capacity and low resistance. As the scanning rate increases, the current density increased, but there are no tangible changes in the shape of the curve, indicating the stability of the material [26, 26].

To evaluate the real applicability of samples for supercapacitors, GCD tests were investigated at various current densities in the -0.1 to 1 V (vs. Ag/AgCl) potential window at different current density. Figure 8a shows the GCD curve of the nanocomposite with several current densities up to 9 A g^{-1} . The specific capacitances of the nanocomposite are thus calculated to be 618, 385, 343, 196 Fg^{-1} at a current density of 4, 8, 9, 18 A g^{-1} , respectively. As can be seen, the specific capacity decreases steadily with increasing current density due to the lack of active material participating in the redox reaction and therefore voltage drop formation at high current density. GCD test of different active materials, including the NRGO, NiCo_2O_4 , and the nanocomposite, is shown in Fig. 8b with an applied constant current density of 9 A g^{-1} to investigate. As can be seen, the nanocomposite has the most discharge time and therefore the most specific capacitances in comparison with pure NiCo_2O_4 and NRGO. This is due to the production of ultrafine NiCo_2O_4 nanoparticles using

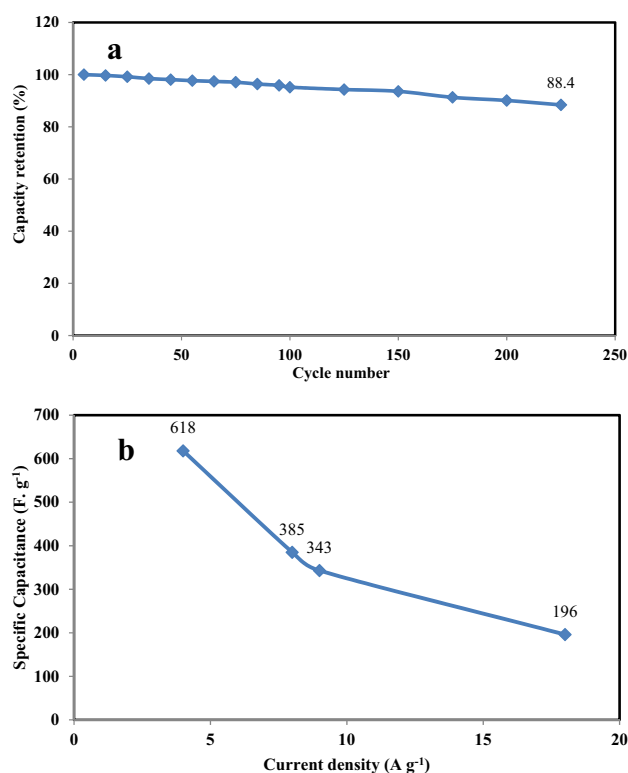


Fig. 9 The cycling stability of the nanocomposite electrode at 4 A g^{-1} **a** and the relationship between the current density of the nanocomposite and the specific capacitance **b**

the sonochemistry method and its nitrogen-doped graphene composite. The cycling stability of the nanocomposite electrode was obtained at 4 A g^{-1} , showing good capacitance retention ratio which is above 88% after 225 charge–discharge cycles (Fig. 9a). Figure 9b illustrates the relationship between the current density of the nanocomposite and the specific capacitance (rate capability of the electrode).

The electron transfer capability of the electrode was studied with the CV of potassium ferrocyanide/ferricyanide redox reactions. For this reason, a solution of $10.0 \text{ mM K}_4[\text{Fe}(\text{CN})_6]$ and 0.10 M KCl was used as the electrolyte in the potential of -0.20 to +0.60 V. For the nanocomposite electrode, less difference between anodic and cathode peak potentials ($\Delta E_p = 0.11 \text{ V}$) and greater current intensity can be seen at the scan rate of 40 mV s^{-1} (Fig. 10a) in comparison with pure NiCo_2O_4 ($\Delta E_p = 0.12 \text{ V}$) confirming better rate of electron transfer and bigger active surface at nanocomposite base of Randles–Sevcik equation. By increasing the scan rate (v) from 20 to 100 mV s^{-1} , the peak current and peak separation potential increase with a gentle slope, indicating quasi-reversible kinetics and diffusion-controlled process at the nanocomposite electrode surface (Fig. 10b) [26].

EIS was used as a very useful technique for studying the interface between electrode and electrolyte. Therefore, EIS experiments were done in a solution of 10.0 mM

Fig. 10 Cycling voltammograms of different electrodes in 10 mM $K_4Fe(CN)_6$ containing 0.1 M KCl at a scan rate of 100 mV s^{-1} . **a**. Cycling voltammograms of nanocomposite electrode in 10 mM $K_4Fe(CN)_6$ containing 0.1 M KCl at different scan rates **b**

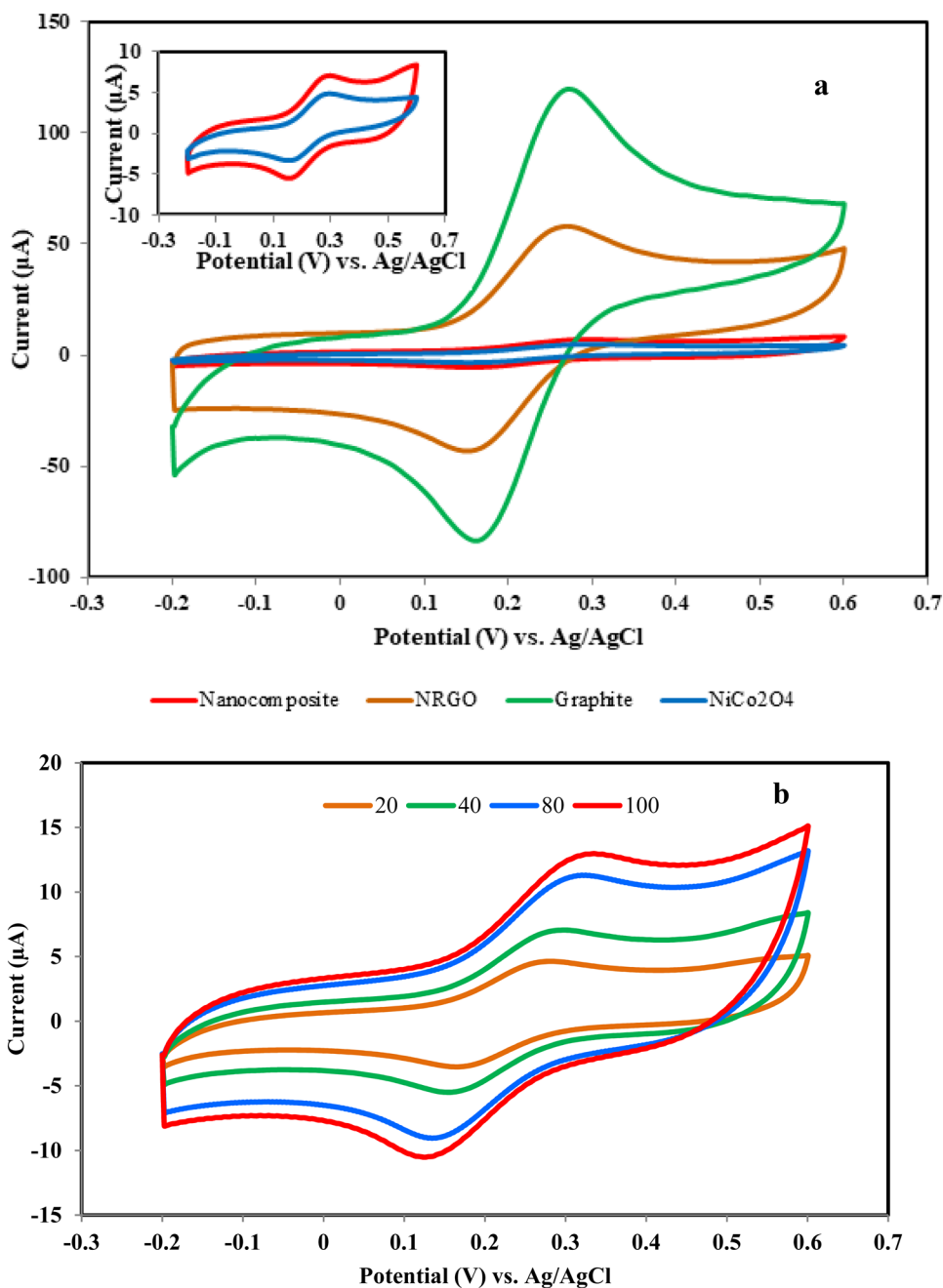


Table 1 Fitting values of the model

| Fitting parameters | NRGO | NiCo ₂ O ₄ | Nanocomposite |
|--------------------|---------|----------------------------------|---------------|
| R_s | 336 | 129 | 132 |
| R_{ct} | 111.3 | 33.78 | 17.66 |
| C_{dl} | 0.00023 | 0.00017 | 0.00051 |
| R_w | 221.1 | 117.7 | 62.23 |
| C_f | 0.00097 | 0.0018 | 0.0029 |

$K_4[Fe(CN)_6]$ and 0.10 M KCl at OCP with an AC perturbation of 5 mV in the frequency range of 0.1 Hz to 100 kHz. The equivalent circuit consists of R_s , R_{ct} , C_{dl} , R_w , and C_f . R_s , internal resistance, is a component of the supercapacitor cell and in the Nyquist plot is the intercept value at the horizontal axis. R_{ct} is a semicircle at high frequency due to kinetic control, and R_w (Warburg impedance) is a straight line at low frequency due to mass transport control. C_{dl} and C_f are double layers and faradic capacitance, respectively

Fig. 11 Nyquist plots of EIS analysis of different electrodes in 10 mM $K_4Fe(CN)_6$ containing 0.1 M KCl and the equivalent circuit model

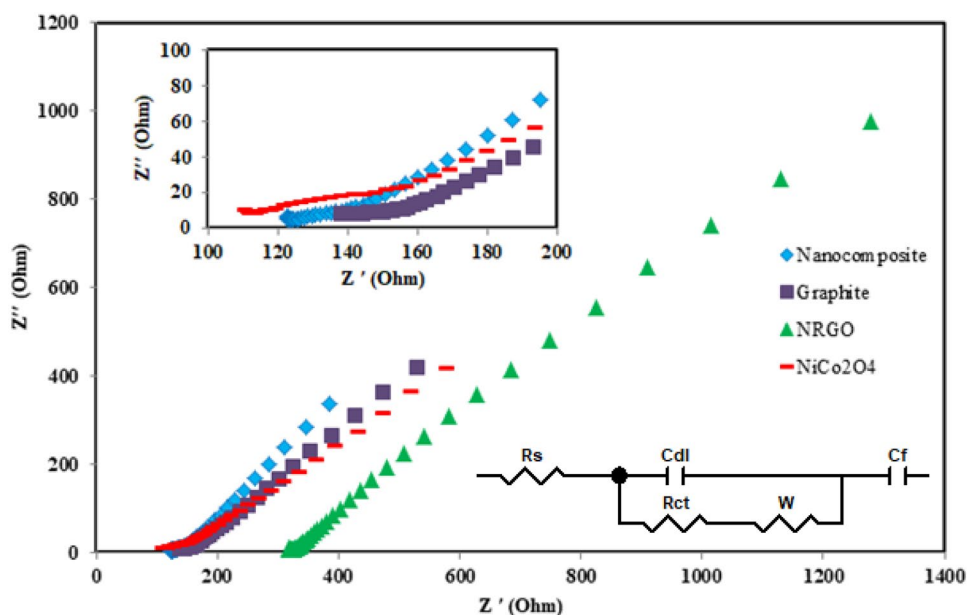


Table 2 Comparison of characteristic performance by the developed method with different $NiCo_2O_4$ -based electrode materials

| Active material | Precursors, time and temperature | Morphology | Synthesis method | Electrolyte | Substrate | Capacity (F/g) | Ref |
|--------------------------|--|----------------------------|------------------|----------------|-----------------|----------------|-----------|
| $NiCo_2O_4$ | $Co(Ac)_2 \cdot 4H_2O$ $Ni(Ac)_2 \cdot 4H_2O$ 3 h., 400°C | Coral-like nanoparticle | Sol-gel | KOH 1 M | Ni foam | 217 | [8] |
| $NiCo_2O_4$ /mesocarbon | $Ni(NO_3)_2 \cdot 6H_2O$ $Co(NO_3)_2 \cdot 6H_2O$, urea 8 h., 95°C | Nanoneedles | Hydrothermal | KOH 3 M | Ni foam | 458 | [26] |
| $NiCo_2O_4$ | $NiCl_2 \cdot 6H_2O$, $CoCl_2 \cdot 6H_2O$ Urea, 6 h., 120°C | Urchin-like nanostructures | Hydrothermal | KOH 3 M | Ni foam | 1348 | [26] |
| $NiCo_2O_4$ | $Co(Ac)_2 \cdot 4H_2O$ $Ni(Ac)_2 \cdot 4H_2O$ CTAB, $NaHCO_3$ 6 h., 35°C | Hollow urchin | Sol-gel | KOH 6 M | Ni foam | 95 | [26] |
| GO/MWCNT/ $NiCo_2O_4$ | $Ni(NO_3)_2 \cdot 6H_2O$ $Co(NO_3)_2 \cdot 6H_2O$ urea, 8 h., 90°C | Nanoparticles | Sol-gel | KOH 6 M | stainless steel | 707 | [26] |
| $NiCo_2O_4$ /NRGO | $Ni(NO_3)_2 \cdot 6H_2O$, $Co(NO_3)_2 \cdot 6H_2O$, urea, CTAB. 25 min., 65°C | Nanoparticles | Sonochemical | Na_2SO_4 1 M | Carbon past | 618 | This work |

[26]. The Zview (version 3.5d) fitting outputs are shown in Table 1. The lines close to the perpendicular indicate the similarity to the ideal capacitor behavior. As can be seen, the slope of the line is higher and the R_w is lower for the nanocomposite (Fig. 11). The diameter of the semicircle is known as R_{ct} which for nanocomposite is the lowest value (17.66 ohms). On the other hand, the higher value for C_{dl} and C_F also can be seen for the nanocomposite, due to the synergistic effect of the NRGO and $NiCo_2O_4$. The above results show the suitable electron transfer, resistive, and capacitive

properties of the desired nanocomposite for use in supercapacitor application.

Conclusions

In the present work, fine $NiCo_2O_4$ nanoparticles and graphite oxide were synthesized by the sonochemical method and modified Hummer methods, respectively. The graphite oxide then reduced and N-doped graphene by a chemical

method using hydrazine and NH_3 solution. The $\text{NiCo}_2\text{O}_4/\text{NRGO}$ nanocomposite was successfully synthesized with ultrasound radiation and characterized using FT-IR, XRD, SEM, and EDX mapping methods. The CV, GCD, and EIS tests were used for capacitance study of the materials. The nanocomposite delivered the highest specific capacitance of 618 F g^{-1} at 4 A g^{-1} current density, with the capacity retention as high as 94% after 100 cycles. Characteristic performance by the developed method was compared with different NiCo_2O_4 -based electrode materials. The results are shown in Table 2. As can be seen, the present nanocomposite shows a straightforward fast sonochemical synthesis procedure for the synthesis of ultrafine nanoparticles and excellent electrochemical performance which are comparable to or better than the others. According to the best of our knowledge, this is the first ultrasonic synthesis of NiCo_2O_4 based on NRGO nanocomposite for use in supercapacitors. Because of the mentioned reasons, it can be ensured that such material can be applied as cathodic electrode material in energy storage devices and large-scale commercial applications.

References

1. A.S. Aricò, P. Bruce, B. Scrosati, J.M. Tarascon, W.V. Schalkwijk, *Nat. Mater.* **4**, 366 (2005)
2. P. Lu, D. Xue, H. Yang, Y. Liu, *Int. J. Smart Nano Mater.* **4**, 2 (2013)
3. P.C. Chen, G. Shen, Y. Shi, H. Chen, C. Zhou, *ACS Nano* **4**, 4403 (2010)
4. A.K. Mondal, D. Su, S. Chen, X. Xie, G. Wang, A.C.S. *Appl. Mater. Interfaces* **6**, 14827 (2014)
5. M. vengari, T. Pryor, L. Jiang, **139**, 72 (2013)
6. F. Fu, J. Li, Y. Yao, X. Qin, Y. Dou, H. Wang, J. Tsui, K. Chan, M. Shao, A.C.S. *Appl. Mater. Interfaces* **9**, 16194 (2017)
7. J. Xu, L. He, W. Xu, H. Tang, H. Liu, T. Han, Y. Zhang, C. Zhang, *Electrochim. Acta* **145**, 185 (2014)
8. Y.Q. Wu, X.Y. Chen, P.T. Ji, Q.Q. Zhou, *Electrochim. Acta* **56**, 7517 (2011)
9. Y. Zhang, Y. Ru, H.L. Gao, S.W. Wang, J. Yan, K.Z. Gao, X.D. Jia, H.W. Luo, H. Fang, A.Q. Zhang, L.Z. Wang, *J. Electrochem. Sci. Eng.* **9**, 243 (2019)
10. C. Wang, E. Zhou, X. Deng, M. Shao, J. Huang, X. Wei, X. Xu, *Sci. Adv. Mater.* **8**, 1298 (2016)
11. M. Chatterjee, S. Saha, S. Das, S.K. Pradhan, *J. Alloy. Compd.* **821**, 1 (2020)
12. J. Du, G. Zhou, H. Zhang, C. Cheng, J. Ma, W. Wei, L. Chen, T. Wang, A.C.S. *Appl. Mater. Interfaces* **5**, 7405 (2013)
13. D. Carriazo, J. Patino, M.C. Gutierrez, M.L. Ferrer, F.d. Monte, *RSC Adv.* **3**, 13690–13695 (2013)
14. S. Hassanpoor, G. Khayatian, A.R.J. Azar, *Microchim. Acta* **182**, 1957 (2015)
15. G. Khayatian, M. Moradi, S. Hassanpoor, *J. Anal. Chem.* **23**, 470 (2018)
16. J.N. Tiwari, R.N. Tiwari, K.S. Kim, *Prog. Mater. Sci.* **57**, 724 (2012)
17. S. Hassanpoor, N. Rouhi, *Int. J. Environ. Anal. Chem.* (2019). <https://doi.org/10.1080/03067319.2019.1669582>
18. J. Chen, B. Yao, C. Li, G. Shi, *Carbon* **64**, 225 (2013)
19. G. Khayatian, M. Jodan, S. Hassanpoor, S. Mohebbi, *J. Iran. Chem. Soc.* **13**, 831 (2016)
20. G.S. Bang, G.W. Shim, G.H. Shin, D.Y. Jung, H. Park, W.G. Hong, J. Choi, J. Lee, S.-Y. Choi, *ACS Omega* **3**, 5522 (2018)
21. D. Long, W. Li, L. Ling, J. Miyawak, I. Mochida, S.H. Yoon, *Langmuir* **26**, 16096 (2010)
22. K. Vytras, I. Švacara, R. Metelka, *J. Serb. Chem. Soc.* **74**, 1021 (2009)
23. S. Zhang, N. Pan, *Adv. Energy Mater.* **5**, 2 (2014)
24. M.E. Uddin, R.K. Layek, N.H. Kim, D. Hui, J.H. Lee, *Compos. B* **80**, 238 (2015)
25. H. Heydari, M.B. Gholivand, *Appl. Phys. A* **187**, 123–133 (2017)
26. M. Barrejón, A. Primo, M.J. Gómez-Escalonilla, J.L.G. Fierro, H. García, F. Langa, *Chem. Commun.* **51**, 16916 (2015)
27. Y. Zhang, Y. Zhang, D. Zhang, L. Sun, *Dalton Trans.* **46**, 9457 (2017)
28. H. Zhang, H. Li, H. Wang, K. He, Y. Shuangyin Wang, J.C. Tang, *J. Power Sour.* **280**, 640 (2015)
29. K. Pandi, M. Sivakumar, S.M. Chen, Y.H. Cheng, T.W. Chen, *Int. J. Electrochem. Sci.* **13**, 1227 (2018)
30. X. Li, X. Xu, F. Xia, L. Bu, H. Qiu, M. Chen, L. Zhang, J. Gao, *Electrochim. Acta* **130**, 305 (2014)
31. Y. Li, W. Gao, L. Ci, C. Wang, P.M. Ajayan, *Carbon* **392**, 1124–1130 (2010)
32. A.K. Das, R.K. Layek, N.H. Kim, D. Jung, J.H. Lee, *Nanoscale* **6**, 10657 (2014)
33. Y. Lei, Y. Wang, W. Yang, H. Yuan, D. Xiao, *RSC Adv.* **5**, 7575 (2015)
34. M.H. Alfaruqi, S. Islam, J. Gim, J. Song, S. Kim, D. Pham, J. Jo, Z. Xiu, V. Mathew, J. Kim, *Chem. Phys. Lett.* **650**, 64 (2016)
35. T.K. Das, S. Banerjee, A. Kumar, A.K. Debnath, V. Sudarsan, *Solid. State. Sci.* **96**, 105952 (2019)
36. Q. Wang, B. Liu, X. Wang, S. Ran, L. Wang, D. Chen, G. Shen, *J. Mater. Chem.* **22**, 21647 (2012)
37. T. Brousse, D.B. Elanger, J.W. Long, *J. Electrochem. Soc.* **162**, A5185 (2015)
38. A.K. Mondel, B. Wang, D. Su, Y. Wang, S. Chen, X. Zhang, G. Wang, *Mater. Chem. Phys.* **143**, 740 (2014)
39. J. Yang, S. Gunasekaran, *Carbon* **51**, 36 (2013)
40. H. Tan, Z. Ren, *Mater. Sci. Forum* **14**, 14 (2016)
41. S. Ramesh, D. Vikraman, H.S. Kim, H.S. Kim, J.H. Kim, *J. Alloy. Compd.* **765**, 369 (2018)